Interplay of sample composition and anomalous Hall effect in Co_xNbS_2

S. Mangelsen,[1,*] P. Zimmer,[1] C. Näther,[1] S. Mankovsky,[2] S. Polesya,[2] H. Ebert,[2] and W. Bensch[1]
[1]*Institute of Inorganic Chemistry, Christian-Albrechts University Kiel, Max-Eyth Straße 2, 24118 Kiel, Germany*
[2]*Department Chemie, Physikalische Chemie, Universität München, Butenandstr. 5–13, 81377 München, Germany*

(Received 3 February 2021; revised 20 April 2021; accepted 21 April 2021; published 7 May 2021)

Herein we present a study on the interplay of chemical composition with respect to x in antiferromagnetic Co_xNbS_2 and the anomalous Hall effect (AHE) in the magnetically ordered state. The AHE diminishes virtually completely in samples with exceeding Co content compared to the idealized composition of $x = 1/3$. For stoichiometric samples the effect is weak but shows a sign reversal just below the magnetic ordering temperature. With increasing deficiency, the magnitude of the AHE compared to the ordinary Hall effect increases and additionally an exchange-biaslike effect can be observed. The results reveal the chemical composition of the samples as tuning parameter for the AHE in Co_xNbS_2. Accompanying first-principles calculations demonstrate that the electronic band structure is only slightly affected by disorder and deficiency of Co, but an impact on the magnetic exchange coupling can be inferred. The results are interesting for the research on 3*d*-metal inserted transition-metal dichalcogenides and in a broader context for the understanding and design of antiferromagnet-based spintronic materials.

DOI: 10.1103/PhysRevB.103.184408

I. INTRODUCTION

Antiferromagnetic materials attract great attention due to their potential applications in future data storage and spintronics [1,2]. One of the interesting properties is the occurrence of an anomalous Hall effect (AHE), which may be used as a readout signal in data storage based on these materials. The AHE is well known for ferromagnetic materials [3] and is generally associated with the net magnetic moment of the sample. In an intuitive approach the effect should vanish in antiferromagnetic materials due to cancellation of the magnetic moments. However, in noncollinear antiferromagnets an AHE can be observed [4–7], which can be explained by real space as well as momentum space approaches [8–10].

The phases Co_xNbS_2 are part of the large family of layered transition-metal dichalcogenides showing chemically variable compositions with the general formula T_xMQ_2 with T = V, Cr, Mn, Fe, Co, Ni, M = Ti, Nb, Ta, and Q = S, Se, all of which show a large phase width with regard to the amount of inserted 3*d* metal [11–16]. These compounds host a plethora of magnetic ordering phenomena that depend on the nature of the layered host and the intercalated 3*d* metal. For $x = 1/4$ and 1/3 the formation of superstructures with an increase of the lattice parameters $a = b$ by a factor of 2 and $3^{1/2}$ can be observed, resulting from the ordered arrangement of the 3*d* metal ions [17–19]. These superstructures can also be observed in samples with deviating stoichiometry [20,21]; however, this requires vacancies on the Wyckoff-sites of the 3*d* metal. More detailed studies have shown that an occupational disorder can be found, which is well documented for samples with the $3^{1/2}$-type superstructure [14,22,23]. The space group in that case is $P6_322$ and the 3*d* metal cations reside ideally only on the 2*c* Wyckoff site (see Fig. 1). In real samples a majority of the 3*d* metal ions resides on that site, while a small but significant amount occupies other available sites in the interlayer space (i.e., 2*b* and 2*d* sites). This occupational disorder affects the balance of magnetic exchange interactions. Considering both the chemical and structural parameters one has multiple degrees of freedom at hand to tune the physical properties of these materials to a significant extent.

Early studies on $Co_{0.33}NbS_2$ already indicated antiferromagnetic order, however with a net ferromagnetic moment that could be induced by an external magnetic field [11]. Later, the magnetic structure was studied and again a net moment in a limited temperature window below T_N was observed. [24] A reexamination of the magnetic structure pointed out an ambiguity between a multidomain magnetic structure with a single propagation vector (q) versus a single-domain structure with multiple q vectors [25]. Only recently an AHE in a small temperature window just below T_N was reported, the coercive field of which follows that of the tiny ferromagnetic moment derived from measurements of the DC magnetization [26]. However, the magnetic moment is far too small to allow for an explanation in the sense of a conventional AHE like in ferromagnetic materials. In addition, the reported collinear magnetic structure [24] cannot explain the AHE. The origin of the effect is rather related to the electronic band structure [26] or to the specific magnetic structure [25,26]. Recent neutron diffraction experiments showed that a multi-q magnetic structure may be present, which can give rise to a large AHE [25]. However, further studies on the actual magnetic structure are needed.

The sensitivity of the magnetic properties to slight changes in stoichiometry was exemplified in some related compounds. For Fe_xNbS_2 with x near 0.33 the emergence of a large exchange bias in Fe-deficient samples was recently reported

*smangelsen@ac.uni-kiel.de

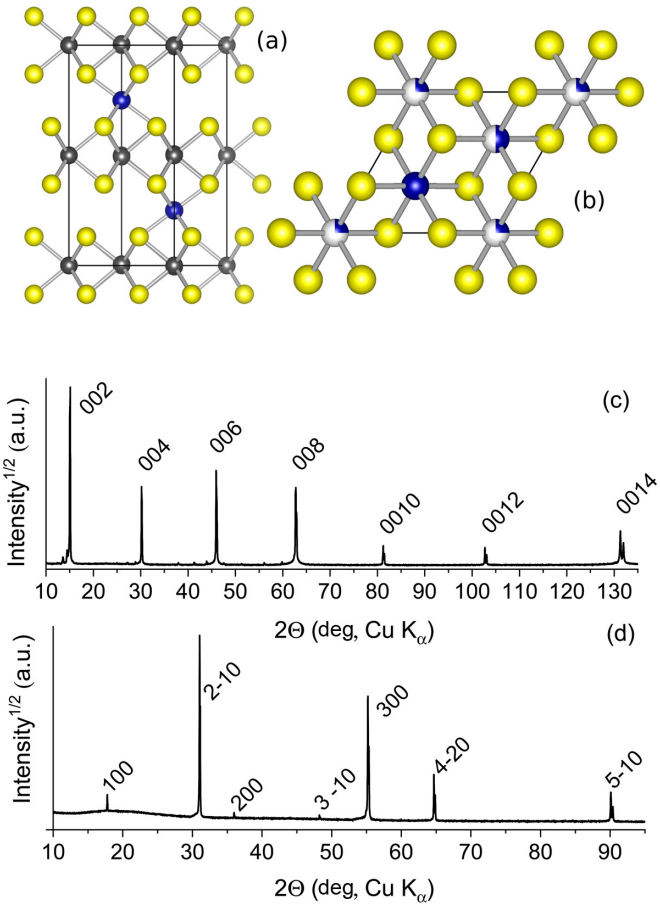

FIG. 1. Idealized structure of $Co_{1/3}NbS_2$ with view along [210] (a) and along [001] with additional available sites for Co [blue color, (b)] [24,49]. The 2*c*-, 2*d*-, and 2*b*-sites are depicted as full, half-filled, and quarter-filled spheres, respectively. Representative XRD patterns using the sample CNS6 as example. XRD carried out on oriented pieces of single crystals showing the 00*l* reflections (c) and pattern showing the *h*00 and *hk*0 reflections (d).

[27]. For ferromagnetic Fe_xTaS_2 the emergence of strong spin-disorder scattering leading to large magnetoresistance was reported [20,28]. Mn_3Sn is an archetypical compound featuring an AHE in noncollinear antiferromagnets. Variations in magnetic order and thus AHE depending on the preparation conditions were reported [29,30]. These findings prompted us to investigate in detail the AHE of Co_xNbS_2 by studying the influence on the AHE by varying the Co content in Co_xNbS_2 using samples with x around 1/3. We demonstrate that the occurrence of the AHE as well as the temperature range of its occurrence are highly sensitive on x. We also found a change of the sign of the anomalous Hall coefficient and the emergence of exchange-biaslike behavior in Co-deficient samples.

II. EXPERIMENT

The crystals were grown from the elements via chemical vapor transport following our previously published procedure [31,32]. A charge of 1 g of the elements (Co: chempur, 99.99%; S: Alfa Aesar, 99.9995%; Nb: chempur, 99.9%) according to different compositions of Co_xNbS_2 were ground and loaded in a silica tube (inner diameter 16 mm) with ∼25 mg of CBr_4 (Fluka, min. 98%) serving as transport agent. The ampoule was evacuated to $p \leqslant 5 \times 10^{-4}$ mbar under cooling with liquid nitrogen to avoid evaporation of CBr_4 and finally was flame sealed. After initial heating to 450 °C for 1 d (boiling point of S) the temperature was raised to 900 °C in an inverted gradient. After a few days the gradient was set to 900→800 °C for chemical vapor transport and crystals of sufficient size (∼1–2 mm in the basal plane) grew within 2 wk. After slow cooling to room temperature within 24 h the ampoules were opened and the crystals were washed with a dilute solution of $Na_2S_2O_3$, water, and acetone. The crystals showed a metallic luster and were stored under vacuum in a desiccator.

X-ray-diffraction (XRD) measurements were performed in reflection geometry on a PANalytical X'Pert Pro MPD equipped with a Göbel mirror using Cu *Kα* radiation. The samples were mounted on a flat stage to collect the 00*l* reflections. For XRD experiments in transmission geometry thin pieces were cut from crystals with a razor blade and further thinned using adhesive tape. The sample thickness was typically below 10 μm which is sufficient for realizing good count statistics in typically 1 h or less. The samples were mounted on adhesive tape and measured on a PANalytical Empyrean diffractometer equipped with a focusing x-ray mirror and Cu *Kα* radiation. The refinement of the lattice parameters was carried out via Pawley fitting using TOPAS ACADEMIC VERSION 6.0 [33].

Single-crystal x-ray diffraction was carried out on a STOE Image Plate Diffraction System (IPDS2) with Mo *Kα* radiation (λ = 0.710 73 Å). A numerical absorption correction was performed using X-RED and X-SHAPE as implemented in the program package X-AREA [34]. The structure was refined starting from the structural model reported by Parkin et *al.* [24] against F^2 using SHELXL-2018 [35] with anisotropic displacement parameters for all atoms. The Co content was refined so that the equivalent isotropic displacement parameters are comparable to that of the other atoms and that the best reliability factors were obtained. All crystals are racemically twinned and therefore, twin refinements were performed. Details of the structure refinement can be found in Table S1 and S2 in the Supplemental Material [36].

Electric transport was measured on rectangular-shaped samples cut from larger crystals, the current was applied in the *ab* plane, and the magnetic field was oriented perpendicular to the layers. Contacts were made with gold wires (50-μm diameter, Heraeus HD2) glued to the samples using silver paint (Acheson 1415, Plano) in four-point geometry. All measurements were carried out on a Quantum Design PPMS9 using the resistivity option. For zero field cooling (*zfc*) measurements the samples were cooled from temperatures well above T_N, typically from $T = 35$ K. Data for field-dependent Hall resistivity (ρ_{xy}) were antisymmetrized except for those datasets showing an exchange-biaslike effect. The magnetization of the sample CNS6 was measured on a stack of four crystals mounted on a quartz stick using the vibrating sample magnetometer option of a PPMS9.

Energy-dispersive x-ray spectroscopy (EDX) was carried out on a Philipps ESEM XL 30 equipped with an EDAX detector. The acceleration voltage was set to 20 keV and data

TABLE I. Collected data for the samples including nominal and measured composition (x in Co_xNbS_2), residual resistivity ratio, and lattice parameter c. The lattice parameter c is 11.95 Å in stoichiometric $2H$-NbS_2 [48]. Standard deviations for x determined by EDX are on the order of ±0.01. Note: Single-crystal data of CNS2 could not be collected as all crystals were too large.

Sample name	Nominal composition (charge)	Measured composition (EDX)	RRR	Lattice parameter c (Å) from 00l series	Lattice parameter c (Å) from single crystal data[a]	Occupancies of 2c/2b sites
CNS1	0.35	0.34	3.9	11.871 33(2)	11.867(3)	0.96/0
CNS2	0.34	0.32	11.8	11.868 (avg)		
CNS3	0.35	0.33	9.9	11.866 6 (avg)	11.868(3)	0.92/0
CNS4	0.33	0.33	4.7	11.864 50(1)	11.858(2)	0.84/0
CNS5	0.32	0.32	2.9	11.868 25 (avg)	11.859(4)	0.93/0
CNS6	0.30	0.30	1.3	11.841 45(6)	11.836(1)	0.69/0.13

[a]Average of two crystals.

on three spots on each crystal were measured (counting time 120 s each) and averaged. Two crystals from each batch were measured and the data showed virtually identical compositions within the limits of the method.

Theoretical investigations on the electronic structure and magnetic properties of $Co_{1/3}Nb_2$ and off-stoichiometric $Co_{0.28}NbS_2$ have been performed using the fully relativistic Korringa-Kohn-Rostoker Green function method [37,38]. The Co concentration of $x = 0.28$ was chosen in order to achieve a significant contrast between the ordered and disordered case. Because calculations based on the local spin density approximation (LSDA) to density functional theory lead to an underestimation of the magnetic moment of Co^{2+} cations in this system, correlation effects have been taken into account via the LSDA+U approach [39,40]. For this the parameters $U = 3.0$ eV and $J = 0.7$ eV and the so-called atomic limit expression [41] for the double-counting corrections have been used. The parametrization for the LSDA exchange and correlation potential as given by Vosko *et al.* [42] was used. A cutoff $l_{max} = 2$ was used for the angular momentum expansion of the Green function. A k mesh with 38 × 38 × 15 points was used for the integration over the Brillouin zone. The chemical disorder due to randomly distributed vacancies on the Co sublattice in $Co_{0.28}NbS_2$ has been treated by means of the coherent potential approximation alloy theory.

To investigate the magnetic properties at finite temperatures, Monte Carlo (MC) simulations have been performed on the basis of the Heisenberg Hamiltonian

$$H = -\sum_{\mathrm{Co}:i,j} J_{ij}^{\mathrm{Co-Co}}(\hat{e}_i \hat{e}_j)$$

taking into account Co-Co exchange interactions within a sphere with radius $R_{max} = 2.5\ a$ (with a being the lattice parameter), i.e., $|R_{ij}| \leqslant R_{max}$. Here $J_{ij}^{\mathrm{Co-Co}}$ are the Co-Co exchange interaction parameters [43], and $\hat{e}_i$ the unit vector characterizing the orientation of the spin magnetic moment on the Co site i.

III. RESULTS AND DISCUSSION

A. X-ray diffraction and sample composition

A series of samples of the nonstoichiometric compounds Co_xNbS_2 (labeled CNS 1–6, see Table I) with varying content of cobalt in the range $x = 0.30$–0.34 were prepared by chemical vapor transport. The variation between initial and final composition according to the EDX data is small and is in the range of −0.01–0.02 for x in Co_xNbS_2 (Table I). Another indicator of sample stoichiometry is the residual resistivity ratio (RRR) ($\rho_{xx,300\,K}/\rho_{xx,2\,K}$). The RRR is maximized around a composition close to the value expected for the idealized superstructures, that is for $x = 1/3$ in this case [21,28]. The values obtained in the present study range from 1.3 (CNS6) to 11.8 (CNS2, see Table I), the latter being much higher than those reported until now which reach only up to RRR ≈ 5 [11,25,26,44]. According to these results, CNS2 exhibits the closest composition near the ideal concentration and order of the Co^{2+} cations.

For all samples XRD patterns on oriented pieces of single crystals were collected such that the reflections of the 00l series and those belonging to the [001] zone axis are collected (see Fig. 1). From the reflection positions of the 00l series, the lattice parameter c was derived, while reflections of the [001] zone axis data give insight into the superstructure that is formed by the Co^{2+} cations in the interlayer space and the lattice parameter $a = b$. Here one has to stress that all samples independent of composition show the 100 reflection at a position indicative of the $3^{1/2}a$-type superstructure. In contrast to c the lattice parameter a is virtually insensitive to the concentration of the intercalant and scatters around 5.765(2) Å (oriented thin slices measured on the Empyrean device) and 5.759(1) Å (single-crystal data collected on the IPDS2 diffractometer, see Table I).

From several studies of related compounds the sensitivity of the lattice parameter c to the amount of inserted 3d metal cations is well documented [21,45–47]. The c-lattice parameter determined from single-crystal datasets and from the 00l reflections collected on the X'Pert instrument are listed in Table I. It is clearly seen that the interlayer distance increases with increasing Co^{2+} content. The samples CNS2-5 exhibit a similar interlayer spacing considering the estimated standard deviations; however, CNS1 and CNS6 can be well differentiated by the lattice parameter c.

In the crystal structure with the space group $P6_322$, the Co^{2+} cations can occupy the three different sites 2b, 2c, or 2d in the interlayer space between successive NbS_2 layers [see Figs. 1(a) and 1(b)]. If one of these sites is fully occupied the chemical composition $Co_{1/3}NbS_2$ results. The single-crystal data refinement of sample CNS1 evidences that the 2c site is almost fully occupied by Co and that no significant occupation

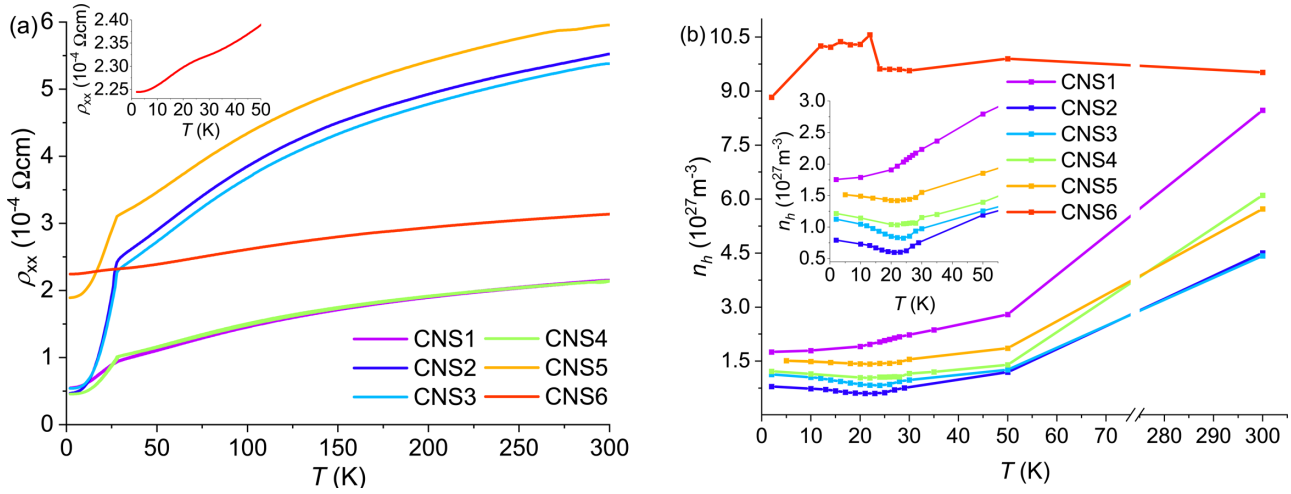

FIG. 2. (a) Temperature-dependent resistivity data of the samples presented in this study. The inset shows an enlarged view of the low-temperature data for sample CNS6. (b) Temperature dependence of the density of charge carriers (holes, n_h) extracted from the Hall effect data (*vide infra*) based on a single carrier model.

on the sites 2*b* and 2*d* is observed. According to the chemical composition of CNS1 with $x = 0.34$ determined by EDX one would expect that one of the other crystallographic sites is also occupied to a low degree. But, the relatively weak intensity of the superstructure reflections, the strong correlation of site occupation factor and displacement parameters, as well as absorption effects prevent a determination of the exact stoichiometry, i.e., the composition derived from single-crystal x-ray data should be interpreted with some care. For the samples CNS3-5 a slight deficiency of the occupation on the 2*c* site is observed in agreement with the off stoichiometry. The most interesting finding is the significant occupation of both the 2*c* and 2*b* sites in the structure of CNS6. This indicates a breakdown of the long-range order of the Co^{2+} cations, where two kinds of structural disorder occur at the same time: missing cations on the 2*c* sites and significant amounts of Co^{2+} cations located on the "wrong" site 2*b*. Because the Co^{2+} cations carry the magnetic moment, this occupation pattern implies that some of the Co^{2+} cations have no neighbor(s) for magnetic exchange interactions, and the structural disorder is likely to induce magnetic frustration.

Summarizing the EDX and XRD data leads to the following structural features: sample CNS1 has a clear excess of Co^{2+}, CNS6 a strong deficiency, and CNS2-5 are well grouped around $x = 1/3$, with CNS2 being closest to the ideal composition. Albeit the very similar results from EDX and the lattice parameter *c*, the RRR makes it possible to distinguish the samples CNS2-5 and this parameter follows the change in initial composition quite closely.

B. Temperature-dependent resistivity

Measurements of the temperature-dependent in-plane resistivity [$\rho_{xx}(T)$, see Fig. 2(a)] reveal a metallicliike behavior with a continuous decrease of the resistivity with decreasing temperature for all samples. Around the magnetic ordering temperature of $T \sim 28$ K there is a prominent drop of the resistivity, which is most pronounced for those samples with *x* near 1/3 (CNS2-5). For the sample with $x \approx 0.30$ (CNS6) only a very broad hump is visible slightly above $T = 20$ K. Also for the sample with $x > 1/3$ (CNS1) a significant broadening of the kink around T_N is evident.

C. Normal Hall effect

In the following the temperature dependence of the normal Hall effect and the resulting carrier concentration will be discussed. The data were extracted from the full part of the isothermal field sweeps above the ordering temperature and from the linear part in the high-field region, in case an AHE was observed (*vide infra*, data in Figs. 3–6). A single band model was assumed to calculate the carrier concentration n_h, which are holes as evidenced by the positive slope of the isothermal field sweeps. A summary of the results is given in Table II, while the temperature-dependent data are presented in Fig. 2(b). All samples show values for n_h ranging from 4.4–9.5 $\times$ 10^{27} m^{-3} at $T = 300$ K. The values are in line with the results reported for $CoNb_3S_6$ ($n_h = 2.49 \times 10^{27}$ m^{-3}

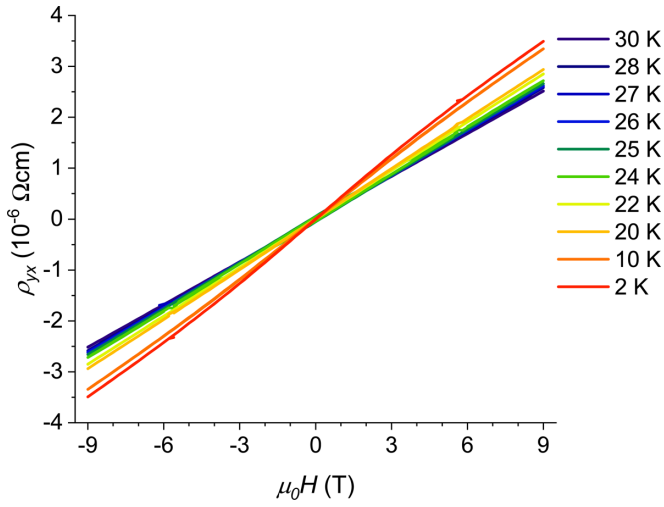

FIG. 3. Isothermal field sweeps of ρ_{xy} for the sample CNS1. Measurement temperatures are indicated.

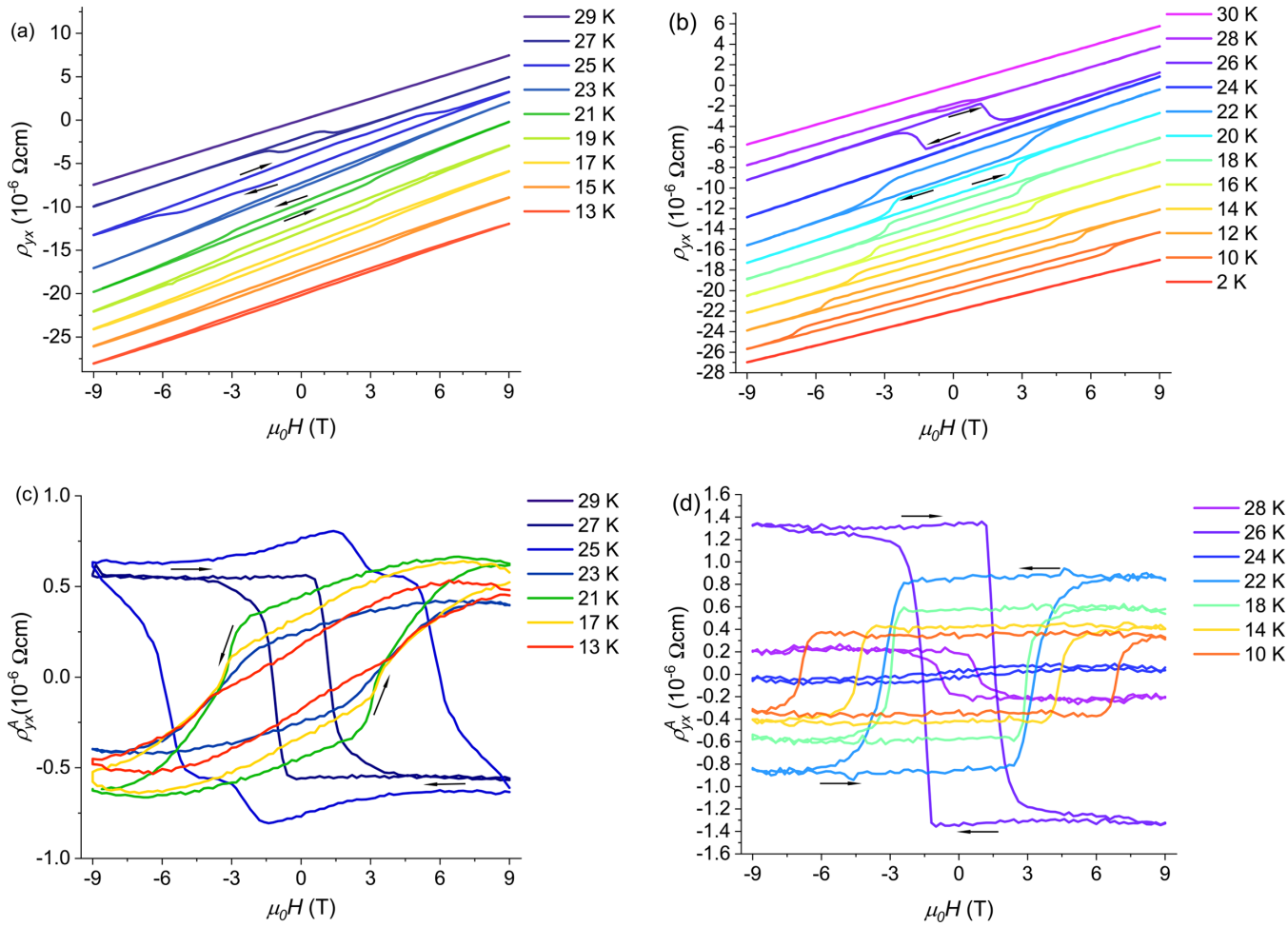

FIG. 4. Isothermal field sweeps of ρ_{xy} for (a) CNS2 and (b) CNS3 (data with vertical offset). Arrows indicate the scanning direction of the magnetic field. Note the sign reversal of the anomalous Hall effect in both cases. Measurement temperatures are indicated. In (c) and (d) the anomalous component $\rho^A{}_{yx}$ of the data presented in (a) and (b) is presented for selected temperatures.

at 28 K) and other related compounds ($Fe_{1/3}TaS_2$: 6.9×10^{27} m^{-3} at 300 K [32], $Cr_{1/3}NbS_2$: 9×10^{26} m^{-3} at 200 K [50], and 2.7×10^{27} m^{-3} at 70 K [51]). Although the errors are fairly large due to the low thickness of the specimens (down to 10 μm), the data suggest a higher carrier concentration for those samples with a Co content deviating significantly from $x = 1/3$. This could be understood by Co^{2+} cations not located on the $2c$ site donating extra charge carriers into the conduction band.

When analyzing the temperature dependence of n_h the sample CNS6 with the largest Co deficiency exhibits a different behavior than the other samples by showing only weak and nonsystematic dependency. This can be attributed to both the Co^{2+} cation disorder of the sample as well as the large contribution of the AHE in the temperature regime below 20 K (*vide infra*, Fig. 5), making the extraction of the normal Hall contribution less reliable. For CNS1 with the largest degree of Co insertion a monotonous decrease of n_h with temperature is observed. In contrast the samples CNS2 and CNS3—having a composition closest to the ideal of $x = 1/3$—display a pronounced minimum of n_h well below the ordering temperature in the range of $T = 21$–25 K. This phenomenon is less pronounced for the samples CNS4 and CNS5 with a significant Co^{2+} deficiency. Thus the appearance of the minimum in carrier concentration appears to be linked to the sample composition. This kind of minimum was reported for other related compounds like $Mn_{1/3}NbS_2$ [51] and $Fe_{1/3}TaS_2$ [32], while from the data in Ref. [52] a maximum of the carrier concentration at $0.5 \times T_C$ can be deduced. It is clear that the magnetic ordering has an impact on the electronic structure; the details however appear to be also dependent on the sample composition. This point will need further attention in future studies, which may be further motivated by the recent findings made for $Cr_{1/3}NbS_2$, where the electronic structure was studied across the magnetic transition via photoemission methods and significant changes in the electronic structure were found [53].

D. Anomalous Hall effect

The extensive measurements of the Hall effect by recording the field-dependent Hall resistivity [$\rho_{yx}(H)$] on all samples reveal a significant dependency of the contribution of the AHE on the Co^{2+} content. The sample containing the largest

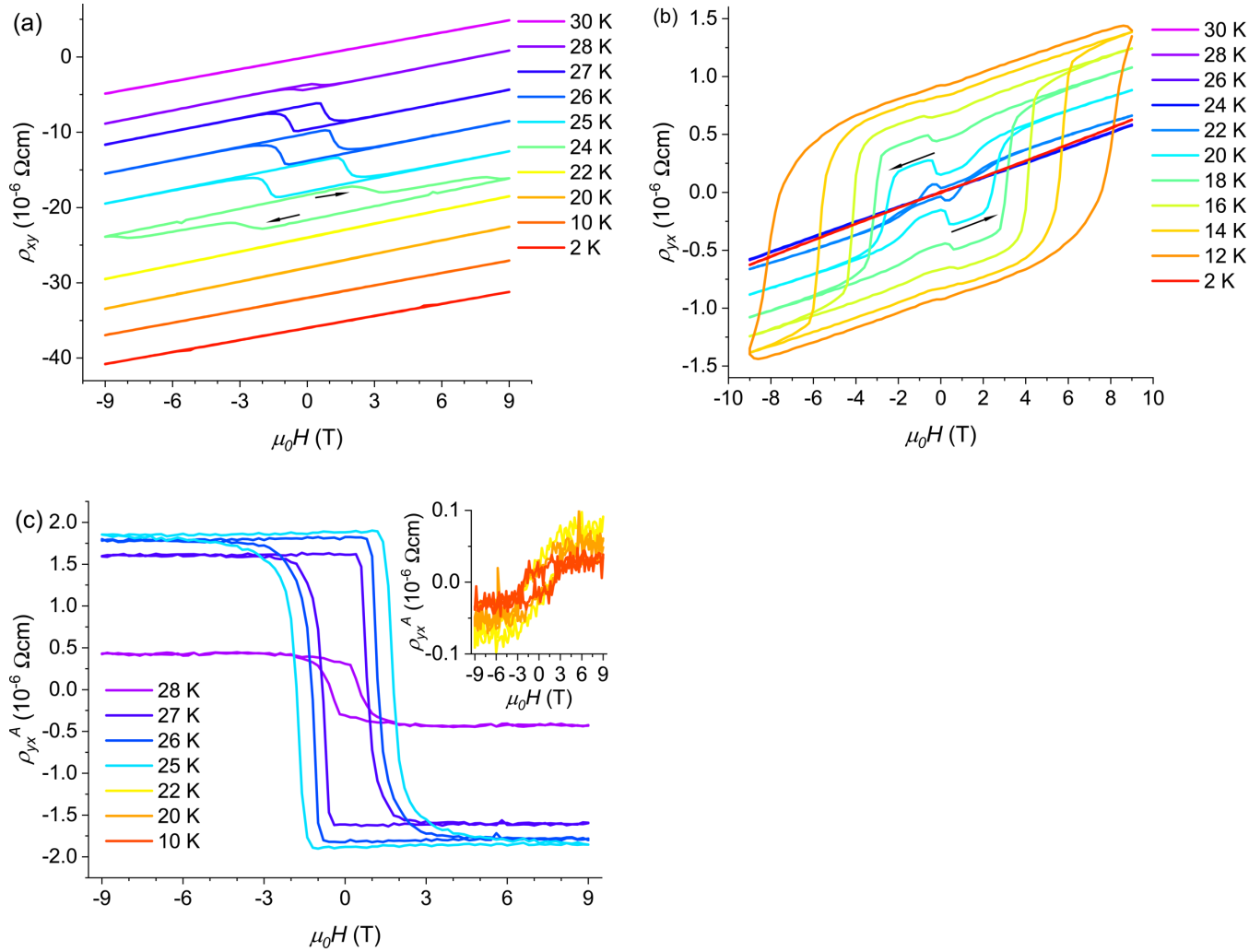

FIG. 5. Isothermal field sweeps of $\rho_{xy}(H)$ for (a) CNS4 (data with vertical offset) and (b) CNS6. Measurement temperatures are indicated. In (c) $\rho^{A}{}_{yx}$ is shown extracted from the data for CNS4 shown in (a); the inset shows the small anomalous component persisting in the temperature range of 22–10 K.

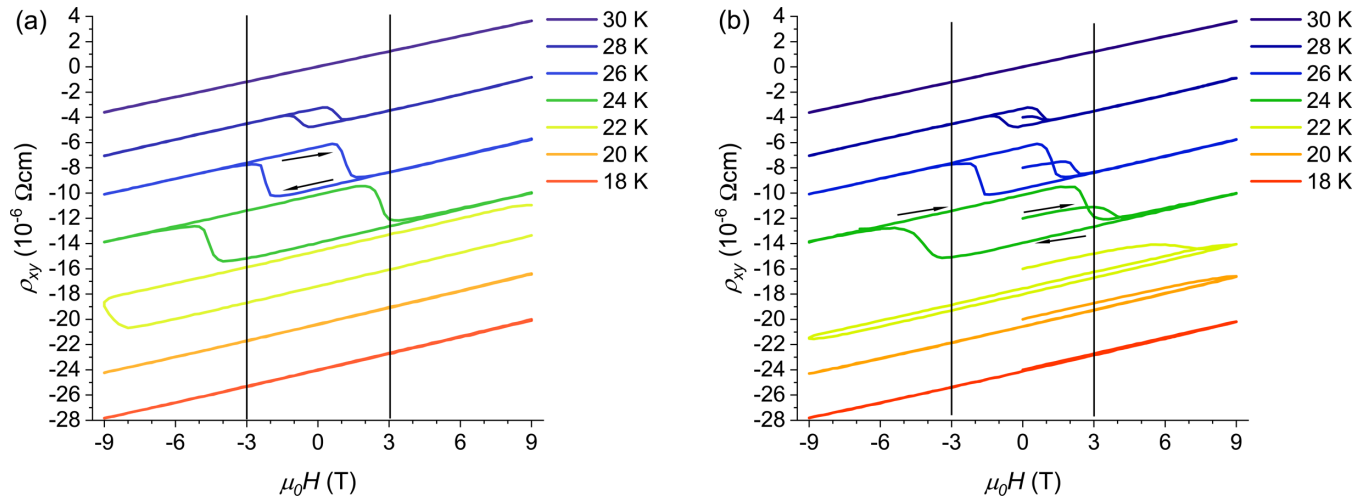

FIG. 6. Field dependence of $\rho_{xy}(H)$ after field cooling with 9 T (a) and in zero field (b) for sample CNS5. Measurement temperatures are indicated. The black vertical bars are a guide to the eye for the shift of the hysteresis loops.

TABLE II. Collected data on the normal and anomalous Hall effect. Errors are estimated based on the inaccuracy in determining the sample thickness.

Sample name	$R_{H,300\,\mathrm{K}}$ (10^{-9} m^3/C)	$n_{h,300\,\mathrm{K}}$ (10^{27} m^{-3})	$\rho^A{}_{yx,\,\mathrm{max}}$ (10^{-6} Ω cm)/sign/temperature (K)
CNS1	0.74 (±0.4)	8.5 (±4)	None detected
CNS2	1.2 (±0.1)	4.5 (±0.4)	0.63/−/25
CNS3	1.4 (±0.7)	4.4 (±2)	1.3 /−/26
CNS4	1.0 (±0.04)	6.1 (±0.2)	1.8 /−/25
CNS5	1.1 (±0.05)	5.7 (±0.3)	1.9 /−/24
CNS6	0.65 (±0.2)	9.5 (±2)	0.9 /+/12

amount of Co^{2+} (CNS1, see Fig. 3) does not show any hysteresis of $\rho_{yx}(H)$ in the temperature interval from $T = 30$ K down to $T = 2$ K. Only a very slight bending of the otherwise straight isotherms is evident at $T \leqslant 10$ K. This could originate from an AHE or from carrier imbalance in the two-carrier model.

For the samples with near-ideal stoichiometry and high RRR values (CNS2 and 3), a hysteresis in the isotherms of $\rho_{xy}(H)$ can be observed at $T \leqslant 28$ K (Fig. 4), which shows a progressive increase of the coercive field with falling temperature, and a negative sign of the AHE coefficient can be inferred from the inverted shape of the hysteresis. There is a sharp change to a positive sign at temperatures of 23–24 K accompanied by an intermediate lowering of the magnitude of the AHE and coercive field. To further highlight this the pure anomalous contribution $\rho^A{}_{yx}$ is presented in Fig. 4(c), which remains after subtracting the normal Hall contribution from the linear portion in the high magnetic field region. Upon further cooling, the AHE remains evident for CNS2 but is quite weak [Figs. 4(a) and 4(c)]. For CNS3 with a slightly lower RRR value the hysteresis loops are clearly developed and again a sign reversal of the AHE can be observed with the effect virtually vanishing at $T = 24$ K. The evolution of the coercive field in the temperature range of 28–20 K shows no clear trend, while there is a continuously increasing coercive field from $T = 20$ K down to $T = 10$ K. The magnitude of the AHE is small [Figs. 4(b) and 4(d)] and at $T = 2$ K no evidence for an AHE is visible. It should be noted that the minimum in the carrier concentration [see Fig. 2(b)] and the sign reversal of the AHE in the samples CNS2 and CNS3 are close in temperature.

The behavior of sample CNS4 [see Figs. 5(a) and 5(c)] is very similar to the data reported by Ghimire et *al.* [26]: A hysteresis indicating an AHE can be observed in the temperature range from 28 to 24 K with progressively increasing coercive fields, while the data measured in the range of $T = 22-10$ K show only a much smaller anomalous contribution to the Hall effect, again with inverted orientation of the hsyteresis [see inset to Fig. 5(c)]. At even lower temperatures down to $T = 2$ K no hysteresis can be observed. The sign of the AHE coefficient is negative in the entire temperature range. The sample CNS6 shows an AHE starting from $T = 22$ K [see Fig. 5 (b)] with progressively increasing anomalous Hall resistivity with a positive coefficient and coercive fields down to $T = 12$ K, where the ferromagnetic component can hardly be saturated. Again at $T = 2$ K no AHE is evident after *zfc vide infra* for data collected after field-cooling (fc) and field-dependent measurements of the magnetic moment. An additional feature that is observed only for sample CNS6 is a contribution to the Hall resistivity that goes beyond the rectangular-shaped AHE. This additional signal leads to a rapid decline of ρ_{xy} upon approaching zero field and a quick rise of $\rho_{xy,AHE}$ towards its previous value after field reversal.

E. Exchange-biaslike behavior

The sample CNS5 displays a similar behavior like CNS4; however, field cooling with +9 T induces a significant exchange-biaslike effect, i.e,. H_c is asymmetric around zero field [see Fig. 6(a)]. At 28 K this effect is insignificant, while at 26 and 24 K an exchange field as large as 1.0 and 2.0 T can be detected. This effect is independent of the cooling conditions [*zfc* or fc, compare Figs. 6(a) and 6(b)] down to $T = 24$ K where H_c can be reached. At $T = 22$ K and below a magnetic field of 9 T is insufficient to saturate the ferromagnetic component and thus only an incomplete irreversible sweep can be observed and differences in the $\rho_{xy}(H)$ curves occur depending on fc or *zfc* cooling. Further typical characteristics of an exchange bias were identified: The effect is reversed under cooling in the opposite field and it has almost vanished in the second isothermal loop [see Fig. 7(a)]. Furthermore, the hysteresis loop can be shifted towards negative or positive magnetic fields depending on the scanning direction of the magnetic field that is applied after *zfc* measurement [Fig. 7(b)].

For the sample CNS6 a significant exchange-biaslike effect at $T = 2$ K [see Fig. 8(a)] is observed, which occurs only after field cooling, in contrast to the observation made for CNS5. A hysteresis loop occurs that is shifted towards the field direction applied for cooling. Furthermore, $\rho_{xy}(H)$ shows a significant offset in total resistivity compared to data of the *zfc* experiment. In order to gain further insight into the underlying magnetic behavior we measured the field-dependent magnetization $M(H)$ at different temperatures [see Fig. 8(b)]. At $T = 30$ K a perfectly linear field dependence is observed, while at $T = 14$ K a small hysteresis loop is found, with an H_c value coinciding with that observed in $\rho_{xy}(H)$ measurements. At a temperature of 2 K after *zfc* neither a hysteresis nor a deviation from linear field dependence can be identified. However, after fc procedure with +9 T of magnetic field a kink in the $M(H)$ trace corresponding to that in $\rho_{xy}(H)$ is evident. The $\rho_{xy}(H)$ and $M(H)$ data recorded after fc in a magnetic field of −9 T only coincide if one assumes a negative sign of the coefficient of the AHE. This

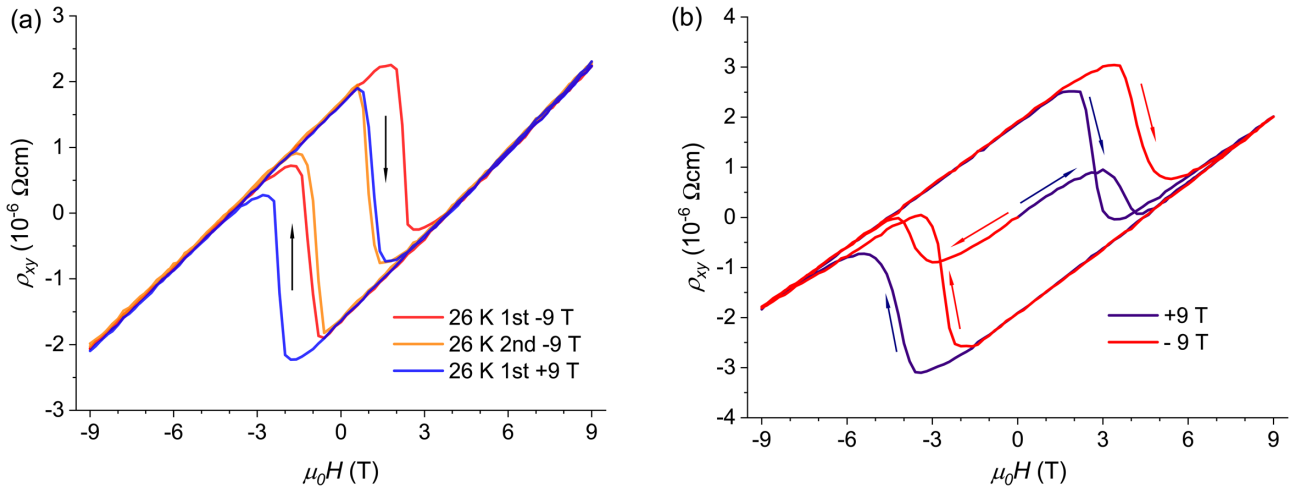

FIG. 7. (a) Data for $\rho_{xy}(H)$ collected on the samples CNS5 at $T = 26$ K after cooling in opposite field directions. The vanishing of the exchange-biaslike effect is demonstrated for field cooling in -9 T of applied magnetic field in a second loop. (b) Scanning of $\rho_{xy}(H)$ at 24 K after *zfc* towards ±9-T magnetic field. Hereby, the dependence of the zero field-exchange bias on magnetization directions is demonstrated.

behavior could be rooted in the formation of oppositely oriented magnetic textures that depend on the field-cooling procedure. However, this phenomenon requires a more detailed inspection in future studies, which is beyond the scope of the present work.

F. Theoretical calculations

As a first step, self-consistent electronic structure calculations have been performed to investigate the ground-state magnetic properties of the ordered compound $Co_{1/3}NbS_2$ (SG $P6_322$) as well as the slightly off-stoichiometric system $Co_{0.28}NbS_2$ with 16% vacancies on the Co sublattice. Figure 9 presents the total density of states (DOS) for $Co_{1/3}NbS_2$ (solid line) in comparison with the DOS for $2H$-NbS_2 (dashed line). The spin-polarized d states of Co (Fig. 9, filled) strongly hybridize with the p states of S as well as d states of Nb, leading to a spin-dependent modification of these states and to a broadening of the valence band for both spin channels. The calculated spin magnetic moment of the Co^{2+} cation is 1.61 μ_B. To see the impact of the deviation from stoichiometry observed in real samples, calculations have been performed also for the system with 16% of vacancies randomly distributed on the Co sublattice. In this case the Co spin magnetic moment decreases to 1.57 μ_B. A small amount of vacancies obviously does not lead to pronounced changes in the electronic structure, and the observed decrease of the magnetic moment can be understood on the basis of the simple rigid-band model. From this one expects that an increase of the vacancy concentration on the Co sublattice is accompanied by a decrease of the number of valence electrons and in turn by a decrease of the valence-band occupation. Because of the

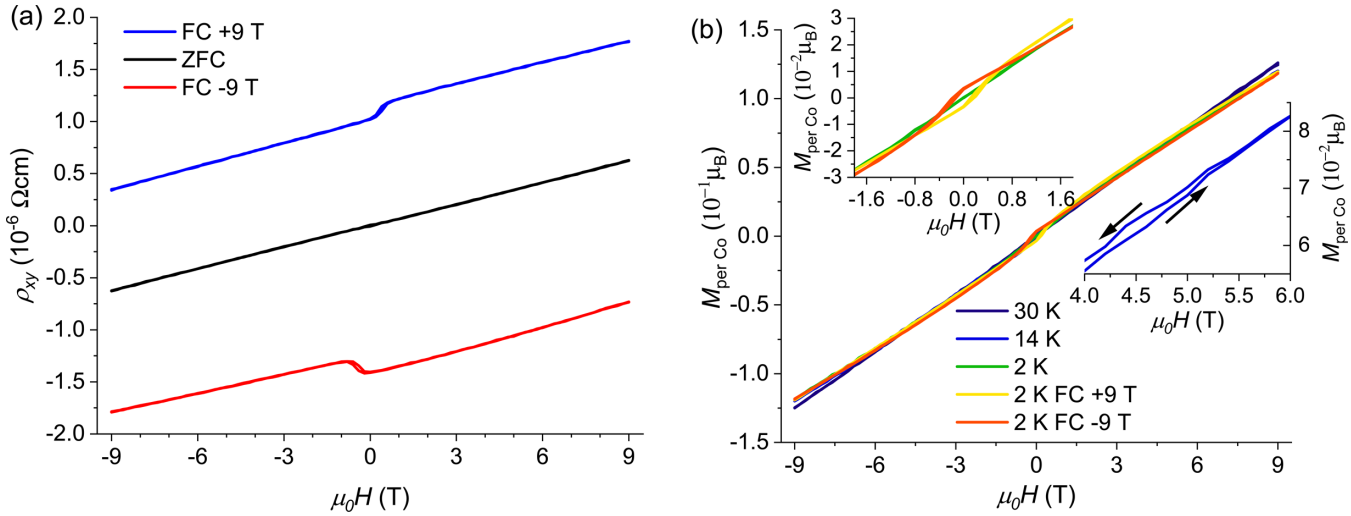

FIG. 8. (a) Exchange-biaslike effect in the Hall resistivity displayed by CNS6 at a temperature of 2 K after cooling in reversed magnetic fields. For zero field cooling no such effect is observed. (b) $M(H)$ traces recorded different temperatures after zero field cooling except indicated differently. The insets show the details of the behavior near zero field at a $T = 2$ K and the small hysteresis loop exemplified at $T = 14$ K, respectively.

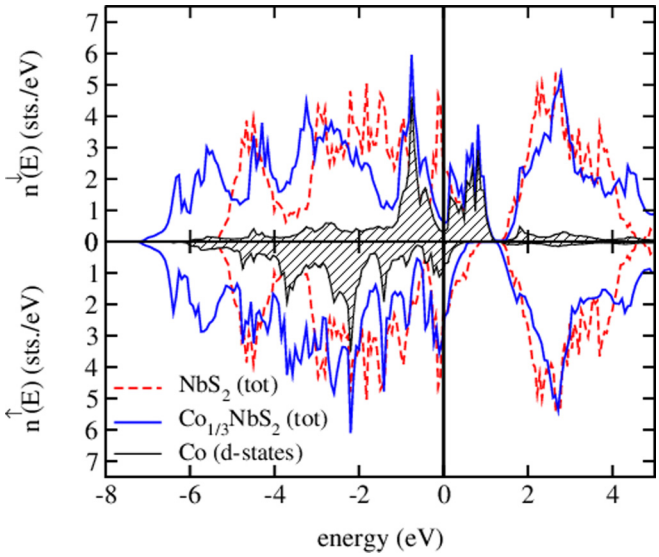

FIG. 9. DOS of Co in the FM-ordered $Co_{1/3}NbS_2$ and the total DOS of $Co_{1/3}NbS_2$ (solid line) compared with the total DOS of $2H$-NbS_2 (dashed line).

dominating DOS at E_F for the states with majority-spin character (see Fig. 9) this decrease of the valence-band occupation results in a decrease of the Co spin magnetic moment.

To gain insight into the differences of the electronic structure for the stoichiometric and nonstoichiometric systems in more detail, Fig. 10 represents the spin-resolved Bloch spectral function $A(E;\,\mathbf{k})$ in the vicinity of the Fermi energy E_F for $Co_{1/3}NbS_2$ and $Co_{0.28}NbS_2$, respectively. In addition to a shift of the Fermi energy, one can see in Figs. 10(c) and 10(d) a weak smearing of the energy bands due to disorder created by the randomly distributed vacancies. This behavior corresponds to a finite lifetime of the electronic states and in turn to a finite residual resistivity at $T = 0\,\mathrm{K}$.

In order to find the ground-state magnetic configuration, the Co-Co exchange coupling parameters J_{ij} have been determined on the basis of the first-principles electronic structure calculations using the formalism reported previously [43]. As the results may depend on the magnetic state of the reference system, the calculations have been performed for the paramagnetic state treated within the disordered local moment (DLM) approximation [54,55]. This approach is generally accepted to give the most reliable critical temperature [54]. The results obtained for $Co_{1/3}NbS_2$ and $Co_{0.28}NbS_2$ are shown in Fig. 11 by closed and open circles, respectively. The nearest-neighbor (*nn*) exchange interactions correspond to a pair of atoms arranged within a Co plane. The values for J_{ij} are negative in this case, indicating the trend to create a noncollinear antiferromagnetic (AFM) alignment of the Co spin moments due to the hexagonal arrangement of the Co^{2+} cations within these layers. The strongest *nnn* exchange parameters represent the interaction between two Co^{2+} cations, which belong to two neighboring Co planes. They are also negative and responsible for the antiparallel alignment of the

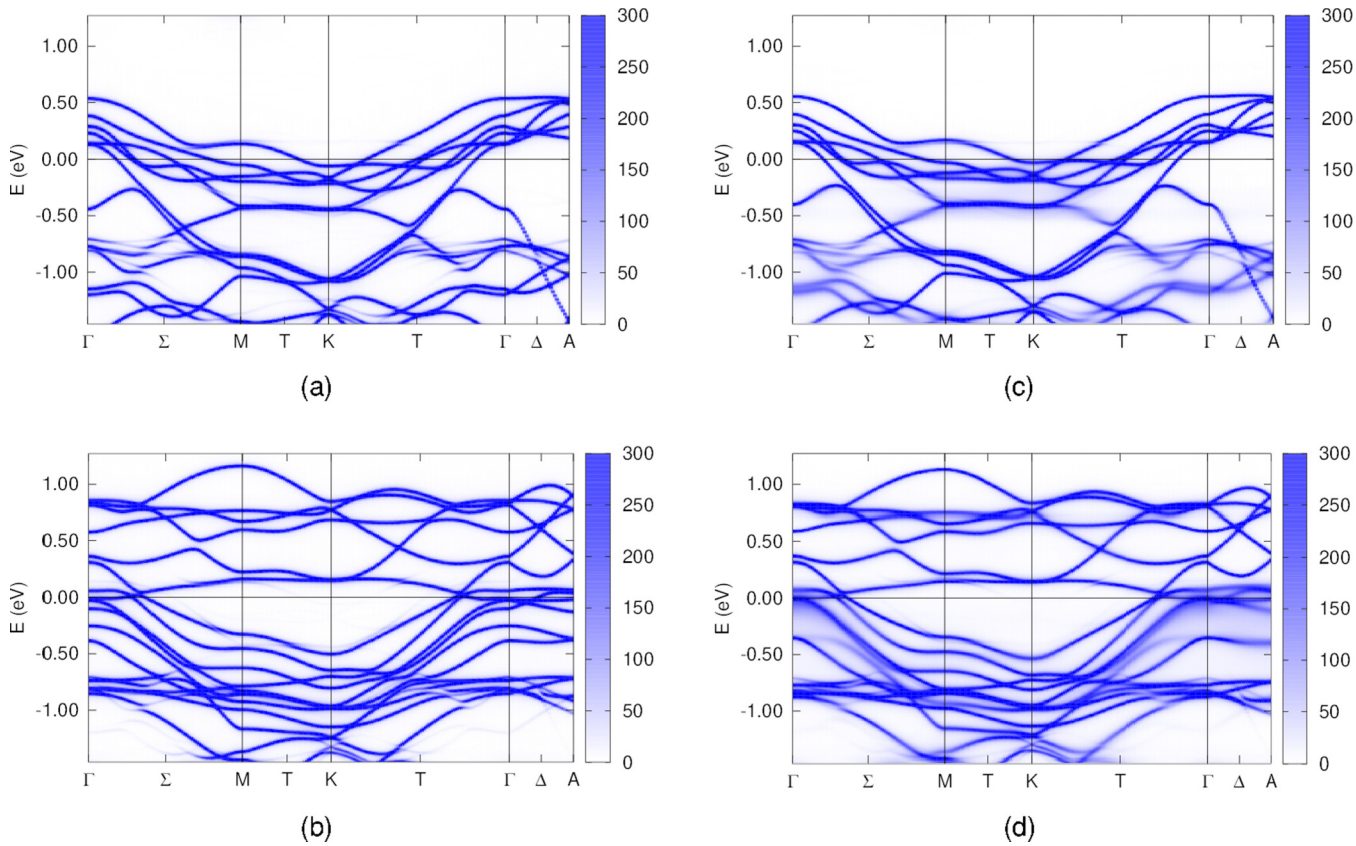

FIG. 10. Spin-resolved Bloch spectral function A (E; k) calculated for stoichiometric $Co_{1/3}NbS_2$ for majority-spin (a) and minority-spin (b) states as well as for the majority-spin (c) and minority-spin (d) states of nonstoichiometric $Co_{0.28}NbS_2$.

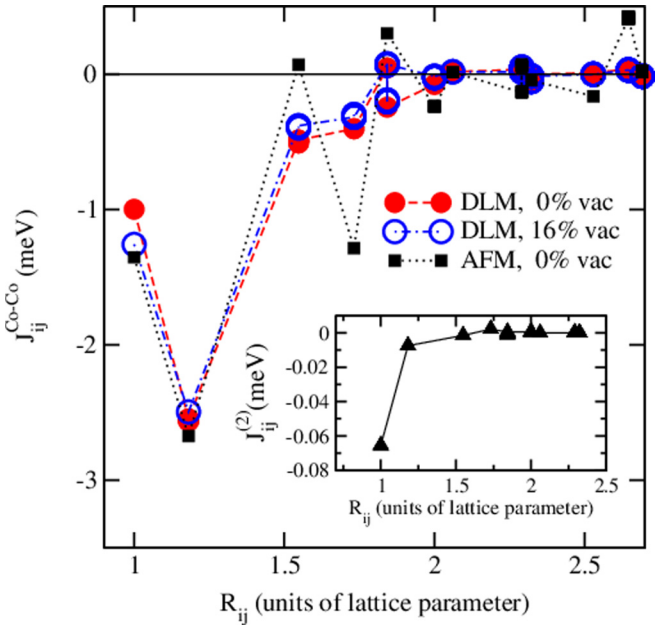

FIG. 11. Interatomic exchange coupling parameter $J_{ij}{}^{\mathrm{Co-Co}}$ calculated for $Co_{1/3}NbS_2$ (closed circles) and for $Co_{0.28}NbS_2$ (open circles) with 16% vacancies on the Co sublattice. Closed squares represent the results obtained for a layer by layer AFM state used as a reference state. The inset shows the biquadratic exchange interactions parameters calculated for $Co_{1/3}NbS_2$ using the DLM reference state.

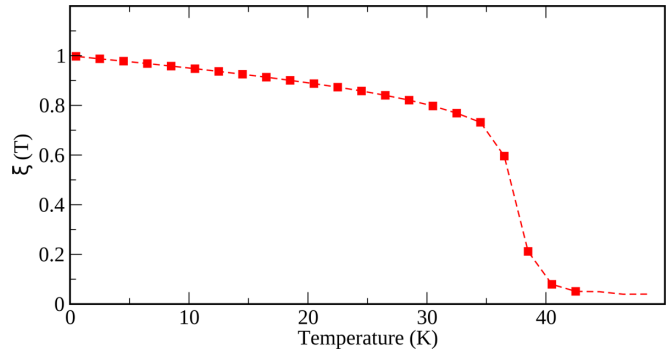

FIG. 12. The order parameter $\xi = 1/2(\langle M_{\mathrm{Co1}}\rangle - \langle M_{\mathrm{Co2}}\rangle)/|M_{\mathrm{Co}}|$ as a function of temperature obtained via MC simulations for $Co_{1/3}NbS_2$.

magnetic moments of neighboring Co planes. Finally, one has to mention a rather strong negative *nnnn* interlayer exchange interaction, with six neighbors in a neighboring Co plane. Obviously, the magnetic structure in this system is a result of a strong competition of the AFM Co-Co exchange interactions at different distances.

To find the equilibrium magnetic configuration below the critical temperature as well as the temperature-dependent magnetization, Monte Carlo simulations have been performed. The critical temperature defined from the temperature-dependent heat capacity is equal to $T = 35$ and $T = 30$ K for $Co_{1/3}NbS_2$ and $Co_{0.28}NbS_2$, respectively. Surprisingly, a competition of all negative Co-Co interactions results in a collinear AFM state with a layer-by-layer AFM ordering. The first-principles calculations of the total energy for the FM and layer by layer AFM states also lead to a stability of the AFM state with an energy difference $E_{\mathrm{tot}}(\mathrm{AFM}) - E_{\mathrm{tot}}(\mathrm{FM}) = -16.5$ meV per formula unit. Figure 12 represents the temperature-dependent order parameter for the AFM state defined as $\xi = 1/2(\langle M_{\mathrm{Co1}}\rangle - \langle M_{\mathrm{Co2}}\rangle)/|M_{\mathrm{Co}}|$ where $\langle M_{\mathrm{Co}i}\rangle$ is the average magnetization of Co1 and Co2 sublattices in the layer by layer AFM configuration. The temperature-dependent electrical resistivity as well as other transport properties are closely connected to the function $\xi(T)$. However, a collinear AFM structure in this material cannot lead to a finite AHE as in this case the system is invariant with respect to time reversal accompanied by rotation and half translation along the c axis.

Having convincing evidence concerning the AFM ground state, Fig. 11 represents also the exchange-coupling parameters calculated using this state as a reference state shown by closed squares in the figure. When compared to the DLM-based results, one can see rather close agreement at small interatomic distances. For larger Co-Co distances, the deviation is more pronounced, which can change a balance in competing contributions to the total energy. As is shown by MC simulations, these interactions lead to a noncollinear magnetic structure well below T_{N}, with a spin modulation within the Co planes, which is characterized by broken time-reversal symmetry. Note however that only the density-functional theory total energy minimization can predict reliable noncollinear magnetic structure. Therefore, further detailed investigations along this line are needed.

In addition, the origin of the noncollinear magnetic structure discussed in the literature can be associated with Dzyaloshinskii-Moriya (DM) and biquadratic (BQ) exchange interactions. These interactions have been calculated [56] for the DLM reference state. The strongest DM interactions $|\mathbf{D}_{ij}| \approx 0.16$ meV occur between the *nnn* Co atoms which belong to neighboring Co layers. The BQ [57] Co-Co interactions, $J^{(2)}{}_{ij}$, shown in the inset of Fig. 11, have the largest magnitude for the *nn* pairs arranged within the same Co planes, $J^{(2)}{}_{01} \approx 0.07$ meV.

IV. DISCUSSION

The above results clearly demonstrate that the AHE in Co_xNbS_2 is remarkably sensitive to the Co^{2+} content. A virtually full suppression of the AHE on the one hand as well as the emergence of additional exchange-biaslike effects and an AHE traceable over a wider temperature range below the ordering temperature are feasible on the other hand. One has to stress that even small differences, e.g., between the samples CNS2 and CNS3 alter the magnitude of the AHE and the corresponding H_c markedly. In previous studies [25,26] on $CoNb_3S_6$ (i.e., $Co_{1/3}NbS_2$) the materials electronic structure and/or a noncollinear multi-q magnetic structure were suggested to be the origin of the AHE in this material. The significant magnetic frustration of the compound [25,58] together with the triangular spin arrangement [24] and the possibly complicated magnetic structure [25] come into play as well.

From the data presented above the question arises: why does the AHE vanish almost completely for the sample CNS1 with an excess of Co^{2+}? One important structural aspect is that—within the limits of the analytic methods—the 2*c* site is virtually fully occupied. This finding implies a complete grid of magnetic cations where the exchange interactions are not disturbed or suppressed by missing cations. The lower RRR value of CNS1 compared to CNS2 (see Table I) suggests that some defects must be present, most likely excess Co^{2+} cations randomly distributed in the interlayer space. Thus disorder alone is not the driving force for the AHE, rather missing Co cations appear to be important as well.

The counterpart is sample CNS6 where both a deficiency and occupational disorder on the Co sites is observed. According to the data obtained from single-crystal diffraction only ∼70% of the 2*c* sites and additionally ∼13% of the 2*b* sites are occupied. This cation distribution pattern likely disturbs the long-range order of the magnetic exchange interactions, which appear to be sensitive to small perturbations, which may be achieved by external pressure [58] or chemical composition and disorder as found in the present study. One has to keep in mind that this is an average structure and local clustering of the magnetic cations cannot be excluded, which was found, e.g., for $Fe_{0.28}TaS_2$ [59]. The exchange-biaslike effect could be related to this type of clustering: The local magnetic clusters might order ferromagnetically and could thus be the origin of both exchange-biaslike phenomenon and AHE. Furthermore, the additional feature observed in low fields in the $\rho_{xy}(H)$ curve [see Fig. 5(b)] together with the apparent change of the sign of the AHE coefficient depending on the field-cooling procedure [Fig. 8(a)] raise the question whether this is possibly rooted in topological magnetic textures.

The changes of the orientation of the hysteresis loops observed in the field sweeps of $\rho_{xy}(H)$ for the samples CNS2, CNS3, and CNS4 [see Figs. 4(a)–4(d) and 5(a) and 5(c)] are another interesting observation. According to the theory of an AHE rooted in a Berry phase resulting from the electronic structure, this would require significant changes of the electronic structure and thus a Berry phase in momentum space. But this appears unlikely, as this small occupational deficiency will rather blur out the electronic bands, which is in line with the calculated band structure for the ordered and disordered case (Fig. 10). A major phase transition cannot be inferred. However, the observed minimum in n_h falling into the same temperature range as the sign reversal of the hysteresis—in particular for CNS2 and CNS3—requires further attention. The reports for $Cr_{1/3}NbS_2$ on changes of the electronic structure [53] and a significant magnetostriction effect across the magnetic ordering temperature [60] raise the question whether also in Co_xNbS_2 more subtle changes in the electronic structure take place across the magnetic ordering. This has to be clarified in future experiments.

Furthermore, a real-space Berry phase originating from spin textures larger than the unit cell seems to be an appealing explanation. These configurations might be prone to reorientation of the spins depending on temperature and emerging magnetic order. This could explain the sign reversal of the AHE observed for the samples CNS2 and CNS3 not far below T_N [see Figs. 4(a)–4(d)] where thermal fluctuations of the spins play an important role. In any case there is a need to further study the magnetic structure of the compounds in this compositional range, in particular also with respect to its temperature dependence below the ordering temperature. The magnetic structure determined at a temperature at 4 K may be correct; however, it cannot account for the observations made regarding the AHE occurring just below T_N. The sensitivity of the interatomic exchange parameters of Co towards the amount of inserted Co is supported by our first-principles calculations (see Fig. 11) and the AFM ground state is well reproduced. While the results depend to some extent on the assumptions made for the calculations, they nevertheless support the hypothesis of a magnetic configuration prone to perturbation. Furthermore, one has to take into account the complex real structure of the crystals with domains of the superstructure having a finite size.

For the sample CNS4 the AHE becomes rapidly very small in magnitude when lowering the temperature from $T = 24\,\mathrm{K}$ to $T = 22\,\mathrm{K}$ and the former progressive increase in H_c is halted [see Figs. 5(a) and 5(c)]. This abrupt change raises the question, what drives the sudden change in the AHE's magnitude? Possibly this is due to a stabilization of the magnetic configuration due to lower thermal excitations. From this point of view the presence of ferromagnetic clusters appears to be unlikely in this sample as those would be static in the crystal and would thus not vanish at lower temperatures.

V. CONCLUSION

Summarizing, we studied a series of samples of Co_xNbS_2 with varying Co content in the range $x = 0.30$–0.34 with respect to the interplay of sample composition, occupation of the octahedral sites in the interlayer space with Co^{2+}, and occurrence of the AHE in the magnetically ordered state. The electric conductivity data demonstrate metallic behavior and the RRR values sensitively depend on the chemical composition. All samples show a drop of the resistivity that is observed around the magnetic ordering temperature, which is more pronounced for samples near the ideal stoichiometry. Further investigations demonstrate that excess Co^{2+} in the samples suppresses the AHE, while a deficiency increases it and makes it observable in a wider temperature range. The data suggest a dependency of the AHE on the occupancy of the 2*c* Wyckoff site in the interlayer space of the crystal structure. A deficiency on these sites would be a viable explanation for a more complex spin arrangement due to magnetic frustration that might drive the AHE. Our first-principles calculations show that occupational disorder and a deficiency of Co^{2+} cations alter the balance of the exchange coupling among these ions. Furthermore, the observed sign reversal of the AHE in samples near $x = 1/3$ and drastic lowering of the magnitude of the AHE at lower temperatures in, e.g., CNS4 point towards a real-space Berry phase as the origin of the AHE.

By means of single-crystal x-ray diffraction only an averaged picture of the structure is obtained; studies on the local domain pattern of the superstructure, e.g., by means of transmission electron microscopy, are needed to clarify the role of local compositional and structural variations. Furthermore, the impact of stoichiometry on the magnetic structure has to be clarified, e.g., whether the reported incommensurate satellites observed by neutron diffraction [25] depend on

stoichiometry or whether larger-scale magnetic textures can be identified. Furthermore, work on the temperature dependence of the magnetic and electronic structure is required. We believe that this work motivates future studies on the magnetic and structural properties of selected samples, as Co_xNbS_2 represents an interesting and tunable system for the relationships between crystal structure and magnetotransport in antiferromagnetic materials. In particular, it will be interesting to see whether static disorder as driving force for magnetic frustration can generally be a tuning parameter for the AHE in antiferromagnetic materials-based spintronics.

ACKNOWLEDGMENTS

Maren Rasmussen and Henning Lühmann are gratefully acknowledged for assistance with measurements at the physical properties measurement system. Financial support by the DFG under Grant No. BE1653/35-1 and by the state of Schleswig-Holstein is gratefully acknowledged for the work carried out in Kiel. H.E., S.P., and S.M. (München) acknowledge financial support from the DFG via Grant No. SFB 1277 and via the DFG Grant No. EB154/36-1.

[1] T. Jungwirth, J. Sinova, A. Manchon, X. Marti, J. Wunderlich, and C. Felser, Nat. Phys. **14**, 200 (2018).
[2] L. Šmejkal, Y. Mokrousov, B. Yan, and A. H. MacDonald, Nat. Phys. **14**, 242 (2018).
[3] N. Nagaosa, J. Sinova, S. Onoda, A. H. MacDonald, and N. P. Ong, Rev. Mod. Phys. **82**, 1539 (2010).
[4] A. K. Nayak, J. E. Fischer, Y. Sun, B. Yan, J. Karel, A. C. Komarek, C. Shekhar, N. Kumar, W. Schnelle, J. Kuebler, C. Felser, and S. S. P. Parkin, Sci. Adv. **2**, e1501870 (2016).
[5] S. Nakatsuji, N. Kiyohara, and T. Higo, Nature (London) **527**, 212 (2015).
[6] T. Suzuki, R. Chisnell, A. Devarakonda, Y.-T. Liu, W. Feng, D. Xiao, J. W. Lynn, and J. G. Checkelsky, Nat. Phys. **12**, 1119 (2016).
[7] Y. Taguchi, T. Sasaki, S. Awaji, Y. Iwasa, T. Tayama, T. Sakakibara, S. Iguchi, T. Ito, and Y. Tokura, Phys. Rev. Lett. **90**, 257202 (2003).
[8] H. Chen, Q. Niu, and A. H. MacDonald, Phys. Rev. Lett. **112**, 017205 (2014).
[9] M. Onoda, G. Tatara, and N. Nagaosa, J. Phys. Soc. Jpn. **73**, 2624 (2004).
[10] J. Kübler and C. Felser, Europhys. Lett. **108**, 67001 (2014).
[11] R. H. Friend, A. R. Beal, and A. D. Yoffe, Philos. Mag. **35**, 1269 (1977).
[12] S. S. P. Parkin and R. H. Friend, Philos. Mag. B **41**, 65 (1980).
[13] S. S. P. Parkin and R. H. Friend, Philos. Mag. B **41**, 95 (1980).
[14] B. Van Laar, H. M. Rietveld, and D. J. W. Ijdo, J. Solid State Chem. **3**, 154 (1971).
[15] M. Inoue, M. Matsumoto, H. Negishi, and H. Sakai, J. Magn. Magn. Mater. **53**, 131 (1985).
[16] H. Negishi, A. Shoube, H. Takahashi, Y. Ueda, M. Sasaki, and M. Inoue, J. Magn. Magn. Mater. **67**, 179 (1987).
[17] J. M. van den Berg and P. Cossee, Inorg. Chim. Acta **2**, 143 (1968).
[18] J. M. Voorhoeve, N. van den Berg, and M. Robbins, J. Solid State Chem. **1**, 134 (1970).
[19] F. Hulliger and E. Pobitschka, J. Solid State Chem. **1**, 117 (1970).
[20] W. J. Hardy, C.-W. Chen, A. Marcinkova, H. Ji, J. Sinova, D. Natelson, and E. Morosan, Phys. Rev. B **91**, 054426 (2015).
[21] A. Le Blanc-Soreau, J. Rouxel, M.-F. Gardette, and O. Gorochov, Mater. Res. Bull. **11**, 1061 (1976).
[22] V. Dyadkin, F. Mushenok, A. Bosak, D. Menzel, S. Grigoriev, P. Pattison, and D. Chernyshov, Phys. Rev. B **91**, 184205 (2015).
[23] A. F. Gubkin, E. P. Proskurina, Y. Kousaka, E. M. Sherokalova, N. V. Selezneva, P. Miao, S. Lee, J. Zhang, Y. Ishikawa, S. Torii, T. Kamiyama, J. Campo, J. Akimitsu, and N. V. Baranov, J. Appl. Phys. **119**, 013903 (2016).
[24] S. S. P. Parkin, E. A. Marseglia, and P. J. Brown, J. Phys. C: Solid State Phys. **16**, 2765 (1983).
[25] G. Tenasini, E. Martino, N. Ubrig, N. J. Ghimire, H. Berger, O. Zaharko, F. Wu, J. F. Mitchell, I. Martin, L. Forró, and A. F. Morpurgo, Phys. Rev. Res. **2**, 023051 (2020).
[26] N. J. Ghimire, A. S. Botana, J. S. Jiang, J. Zhang, Y.-S. Chen, and J. F. Mitchell, Nat. Commun. **9**, 3280 (2018).
[27] S. Doyle, C. John, E. Maniv, R. A. Murphy, A. Maniv, S. K. Ramakrishna, Y.-L. Tang, R. Ramesh, J. R. Long, A. P. Reyes, and J. G. Analytis, arXiv:1904.05872, (2019).
[28] C.-W. Chen, S. Chikara, V. S. Zapf, and E. Morosan, Phys. Rev. B **94**, 054406 (2016).
[29] N. H. Sung, F. Ronning, J. D. Thompson, and E. D. Bauer, Appl. Phys. Lett. **112**, 132406 (2018).
[30] E. Krén, J. Paitz, G. Zimmer, and É. Zsoldos, Physica B+C **80**, 226 (1975).
[31] S. Polesya, S. Mankovsky, H. Ebert, P. G. Naumov, M. A. ElGhazali, W. Schnelle, S. Medvedev, S. Mangelsen, and W. Bensch, Phys. Rev. B **102**, 174423 (2020).
[32] S. Mangelsen, J. Hansen, P. Adler, W. Schnelle, W. Bensch, S. Mankovsky, S. Polesya, and H. Ebert, J. Phys. Chem. C **124**, 24984 (2020).
[33] A. A. Coelho, J. Appl. Crystallogr. **51**, 210 (2018).
[34] *X-Area* (STOE & CIE GmbH, Darmstadt, Germany, 2008).
[35] G. M. Sheldrick, Acta Crystallogr., Sect. C: Struct. Chem. **71**, 3 (2015).
[36] See Supplemental Material at http://link.aps.org/supplemental/10.1103/PhysRevB.103.184408 for details of the single-crystal structure refinements.
[37] H. Ebert *et al.*, The Munich SPR-KKR Package (Munich, 2017), https://www.ebert.cup.uni-muenchen.de/old/index.php?option=com_content&view=article&id=8&catid=4&Itemid=7.
[38] H. Ebert, D. Ködderitzsch, and J. Minár, Rep. Prog. Phys. **74**, 096501 (2011).
[39] A. B. Shick, A. I. Liechtenstein, and W. E. Pickett, Phys. Rev. B **60**, 10763 (1999).
[40] A. N. Yaresko, V. N. Antonov, and P. Fulde, Phys. Rev. B **67**, 155103 (2003).
[41] M. T. Czyżyk and G. A. Sawatzky, Phys. Rev. B **49**, 14211 (1994).

[42] S. H. Vosko, L. Wilk, and M. Nusair, Can. J. Phys. **58**, 1200 (1980).
[43] H. Ebert and S. Mankovsky, Phys. Rev. B **79**, 045209 (2009).
[44] N. Barišić, I. Smiljanić, P. Popčević, A. Bilušić, E. Tutiš, A. Smontara, H. Berger, J. Jaćimović, O. Yuli, and L. Forró, Phys. Rev. B **84**, 075157 (2011).
[45] M. Nakayama, K. Miwa, H. Ikuta, H. Hinode, and M. Wakihara, Chem. Mater. **18**, 4996 (2006).
[46] H. Hinode, T. Ohtani, and M. Wakihara, J. Solid State Chem. **114**, 1 (1995).
[47] H. Narita, H. Ikuta, H. Hinode, T. Uchida, T. Ohtani, and M. Wakihara, J. Solid State Chem. **108**, 148 (1994).
[48] W. G. Fisher and M. J. Sienko, Inorg. Chem. **19**, 39 (1980).
[49] K. Momma and F. Izumi, J. Appl. Crystallogr. **44**, 1272 (2011).
[50] A. C. Bornstein, B. J. Chapman, N. J. Ghimire, D. G. Mandrus, D. S. Parker, and M. Lee, Phys. Rev. B **91**, 184401 (2015).
[51] S. K. Karna, F. N. Womack, R. Chapai, D. P. Young, M. Marshall, W. Xie, D. Graf, Y. Wu, H. Cao, L. DeBeer-Schmitt, P. W. Adams, R. Jin, and J. F. DiTusa, Phys. Rev. B **100**, 184413 (2019).
[52] J. G. Checkelsky, M. Lee, E. Morosan, R. J. Cava, and N. P. Ong, Phys. Rev. B **77**, 014433 (2008).
[53] N. Sirica, P. Vilmercati, F. Bondino, I. Pis, S. Nappini, S.-K. Mo, A. V. Fedorov, P. K. Das, I. Vobornik, J. Fujii, L. Li, D. Sapkota, D. S. Parker, D. G. Mandrus, and N. Mannella, Commun. Phys. **3**, 65 (2020).
[54] B. L. Gyorffy, A. J. Pindor, J. Staunton, G. M. Stocks, and H. Winter, J. Phys. F: Met. Phys. **15**, 1337 (1985).
[55] B. L. Györffy, A. Barbieri, J. B. Staunton, W. A. Shelton, and G. M. Stocks, Phys. B **172**, 35 (1991).
[56] S. Mankovsky and H. Ebert, Phys. Rev. B **96**, 104416 (2017).
[57] S. Mankovsky, S. Polesya, and H. Ebert, Phys. Rev. B **101**, 174401 (2020).
[58] P. Popčević, I. Batistić, A. Smontara, K. Velebit, J. Jaćimović, E. Martino, I. Živković, N. Tsyrulin, J. Piatek, H. Berger, A. A. Sidorenko, H. M. Rønnow, N. Barišić, L. Forró, and E. Tutiš, arXiv:2003.08127 (2020).
[59] M. Eibschütz, F. J. DiSalvo, G. W. H. Jr., and S. Mahajan, Appl. Phys. Lett. **27**, 464 (1975).
[60] T. Tajiri, M. Mito, Y. Kousaka, J. Akimitsu, J.-i. Kishine, and K. Inoue, Phys. Rev. B **102**, 014446 (2020).